Novel Structure for High Performance UV Photodetector Based on BiOCl/ZnO Hybrid Film

*Feng Teng, Weixin Ouyang, Yanmei Li, Lingxia Zheng, and Xiaosheng Fang**

***A** novel type of high performance ultraviolet (UV) photodetector (PD) based on a ZnO film has been prepared by incorporating a BiOCl nanostructure into the film. The responsivity of the BiOCl/ZnO hybrid film PD in UV region can reach 182.87 mA W^{-1}, which is about 2.72 and 6.87 times for that of TiO_2/ZnO hybrid film PD and pure ZnO film PD. The rise/decay time of BiOCl/ZnO hybrid film PD is 25.83/11.25 s, which is much shorter than that of TiO_2/ZnO hybrid film PD (51.94/26.05 s) and pure ZnO film PD (69.34/>120 s). The BiOCl nanostructure can inject photogenerated electrons into the ZnO film under UV light illumination, leading to the increase of photocurrent, and forms barriers to block the straight transmission of electrons between electrodes, resulting in the decrease of decay time. The results of control experiment show that the transfer path of photogenerated electrons formed by p–n junction will be cut off after depositing gold nanoparticles on the film surface, which means this hybrid film is a unique and novel structure to improve the optoelectronic performance of photodetectors. This novel BiOCl/ZnO hybrid structure paves new route for the development of film PDs based on ZnO film.*

1. Introduction

Ultraviolet (UV) radiation has been regarded as one important component of the solar radiation and is divided into three bands by the International Commission on Illumination. Although the ozone layer at the outermost layer of the earth's atmosphere can block the majority of UV-C ($100 \le \lambda < 280$ nm) radiation off, UV-B ($280 \le \lambda < 320$ nm) and UV-A ($320 \le \lambda < 400$ nm) radiation can still reach the earth's surface and become the culprit for many diseases, including erythema, DNA damage, apoptotic cell death, skin pigmentation, and skin cancer.[1–3] UV photodetector (PD) which transfer UV radiation signals to electrical ones plays an important role in the field of radiation warning, flame detection, missile tracking, and encrypted signal transmission.[4–8] Among a large variety of sensitive materials (such as SnO_2,[5] TiO_2,[6] Nb_2O_5,[7] etc.) for UV PDs, ZnO as an environment-friendly semiconductor with a band gap of ≈3.37 eV at room temperature draws great attention.[9–11] Various ZnO nanomaterials were used to construct metal–semiconductor–metal type UV PDs because of their high photoconductive characteristics.[12–15] In particular, ZnO nanofilm exhibits its great potential in PDs due to its ease of fabrication, high transparency, significant on/off switching, large device area, physical flexibility, and low cost.[16–18]

For the film PD made from ZnO nanoparticles (NPs), its large surface-to-volume ratio allows great amount of oxygen molecules to adsorb onto the ZnO surface, resulting in the generation of a low-conductivity depletion layer on each nanoparticle, which leads to the current attenuation when the UV light is off.[19,20] Due to the slow adsorption/desorption rate of oxygen molecules, long rise/decay time is always observed for ZnO film PDs, which becomes the biggest obstacle for their practical application. Therefore, many efforts have been devoted to shortening the response time in recent years. Tailoring the depletion layer on the ZnO NP surface is a common method. For instance, Jin et al. recently prepared a ZnO film PD with graphdiyne (GD) covering on the surface of ZnO NPs with a high responsivity of 1260 A W^{-1} and short rise/decay time of 6.1/2.1 s (10 V bias and 365 nm UV light illumination) due to a p–n junction formed at the interface between ZnO NP and GD NPs, which expanded

Dr. F. Teng, W. X. Ouyang, Y. M. Li,
Dr. L. X. Zheng, Prof. X. S. Fang
Department of Materials Science
Fudan University
Shanghai 200433, P. R. China
E-mail: xshfang@fudan.edu.cn

DOI: 10.1002/smll.201700156

the depletion region near the ZnO surface and led to the rapid current decline when the light was turned off.[16] Similarly, it is also feasible to adjust the depletion layer of ZnO nanorod-based PD to optimize the photoresponse performance by controlling the nanojunction between neighboring nanowires.[21] Modifying the surface of nanorods with other materials (e.g., ZnS,[22] gold nanoparticles,[23] and poly(vinyl alcohol)[24]) also has significant effect on the enhanced performance of PDs. However, modification of every single nanoparticle or nanorod with other materials is a complex engineer, which is not suitable for the easy fabrication of ZnO film PDs, even if without taking the cost of these materials into consideration. Effective and simple structures need to be designed and constructed for a new generation of film PDs.

Another promising strategy is to extend the transport path of electrons in order to accomplish short response time by constructing heterojunction composite, such as type II heterojunction structures. Considering the absorption of visible light for the semiconductors with narrow band gap, the band gap of the chosen semiconductor material should be similar to that of ZnO. As typical wide band gap semiconductor materials, BiOCl[25,26] and TiO_2 have been chosen to be introduced into ZnO films and form type II heterojunction, which would form barriers (or traps) of electrons and achieve the decrease of response time. Herein, novel hybrid structures of BiOCl/ZnO film and TiO_2/ZnO film are prepared by a facile spin-coating method and constructed to PDs. Compared with the obtained TiO_2/ZnO hybrid film PD, the BiOCl/ZnO film PD exhibits excellent optoelectronic properties, including higher photocurrent/responsivity and shorter response time, outperforming the pristine ZnO film PD counterpart. And considering the influence of BiOCl in the film, the BiOCl/ZnO hybird film with different contents of BiOCl and calcined at different temperatures have been further studied. In addition, gold nanoparticle decoration is also investigated to enhance the optoelectronic performance of BiOCl/ZnO film devices.

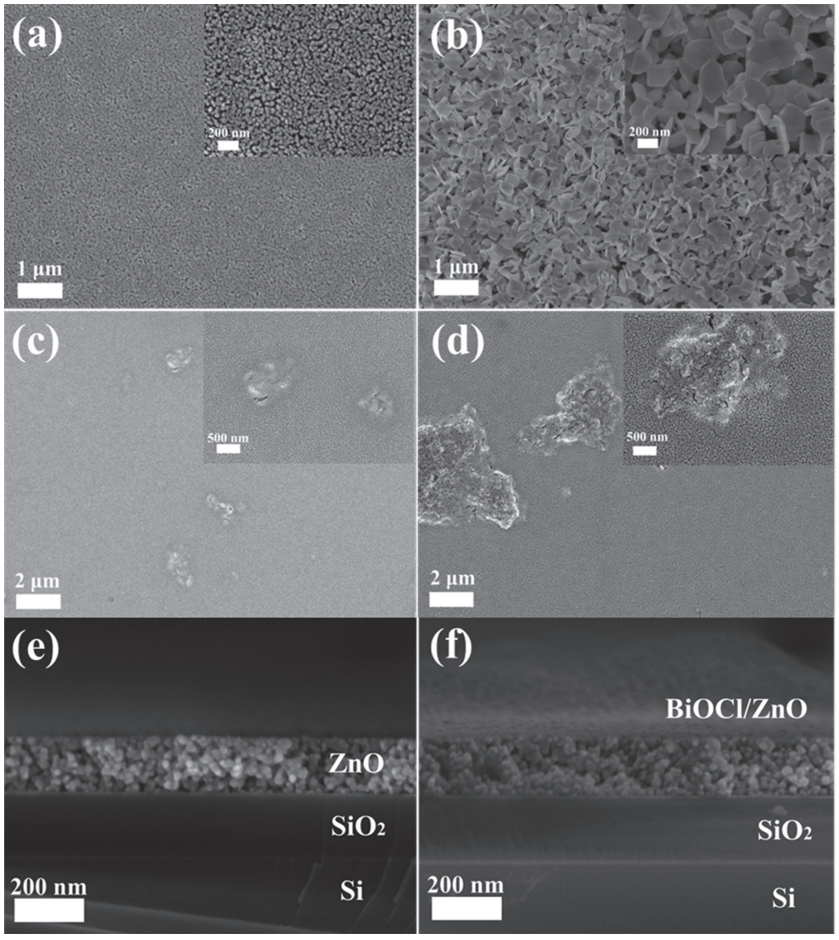

Figure 1. Plane-view SEM images of a) ZnO film, b) BiOCl nanosheets, c) BiOCl/ZnO hybrid film, and d) TiO_2/ZnO hybrid film. And side-view SEM images of e) ZnO film and f) BiOCl/ZnO hybrid film.

2. Results and Discussion

The morphology of the prepared ZnO film, BiOCl nanosheets, BiOCl/ZnO hybrid film, and TiO_2/ZnO hybrid film were examined by a scanning electron microscopy (SEM), and the obtained SEM images are shown in **Figure 1**. The pristine ZnO film shows good uniformity, consisting of a large amount of nanograins with size ranging from several nanometers to hundreds of nanometers (Figure 1a). The obtained BiOCl nanosheets exhibit uniform sizes with an average size of 300 nm and thickness of 40 nm (Figure 1b and Figure S1a (Supporting Information)). The BiOCl/ZnO hybrid film was obtained by spin-coating a mixture of certain amount of BiOCl nanosheets and the ZnO precursor solution to a glass substrate, and then performing the calcination treatment. As shown in Figure 1c, the BiOCl nanosheets are randomly intercalated into the ZnO film and tend to form nanoparticle clusters due to heat treatment, which strongly destroys the flatness of the film (Figure S1b–d, Supporting Information). For comparison, the TiO_2/ZnO hybrid film was prepared and its structure is revealed in Figure 1d. Similarly, the TiO_2 nanoparticles also aggregate into large clusters and demonstrate a random distribution. To better determine the thickness of the prepared ZnO film and BiOCl/ZnO hybrid film, both samples were prepared on Si substrates with 200 nm thick SiO_2 top layer. The cross-sectional SEM images indicate that the ZnO film have a very flat surface with a thickness of 160–180 nm, while the thickness of BiOCl/ZnO film keeps constant (Figure 1e,f).

The crystalline structures of the ZnO film, TiO_2 nanoparticles, BiOCl nanosheets, and BiOCl/ZnO hybrid film calcined at 450 °C were confirmed by X-ray diffraction (XRD) patterns (**Figure 2**a and Figure S1 (Supporting Information)).

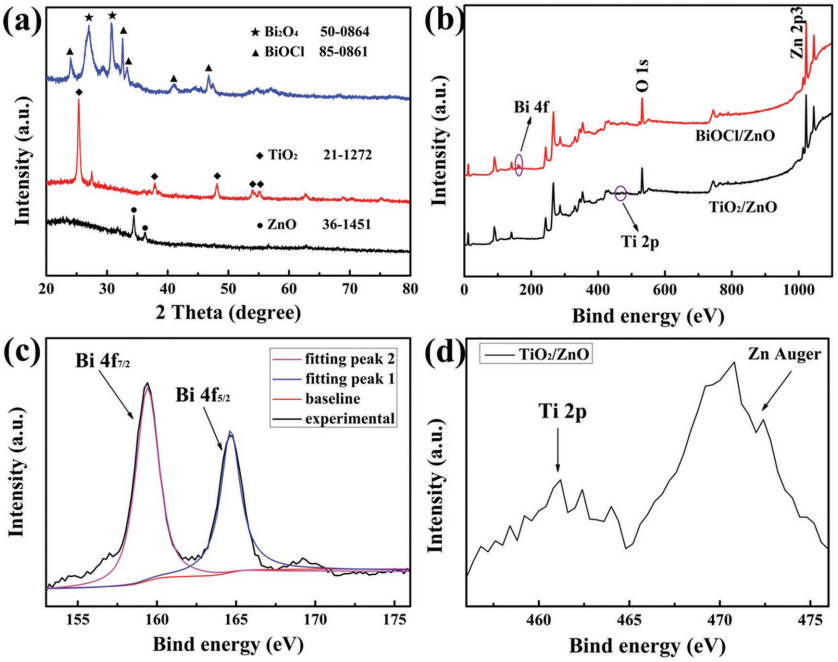

Figure 2. a) XRD patterns of the ZnO film (black line), TiO_2 nanoparticles (red line), and BiOCl nanosheets (blue line). XPS spectra of the TiO_2/ZnO and BiOCl/ZnO film: b) survey scan, c) Bi 4f, and d) Ti 2p spectrum.

For ZnO film, two peaks located at 34.42° and 36.25° are well matched with the (002) and (101) plane of ZnO (JCPDS No. 36-1451), respectively, in good agreement with our previous study.[27] The peaks of TiO_2 nanoparticles at 25.0°, 37.8°, 48.0°, 53.9°, and 55.1° are assigned to (101), (004), (200), (105), and (211) reflection planes of the anatase phase of TiO_2, respectively. A weak peak at 27.4° is attributed to the (110) plane of rutile TiO_2. All the diffraction peaks are consistent with the XRD patterns of Degussa P25.[28] For BiOCl nanosheets, seven peaks at 24.1°, 25.8°, 32.5°, 33.5°, 34.8°, 40.9°, and 46.7° are agreed well with the tetragonal BiOCl structures,[29] while other two at 26.8° and 30.3° are assigned to Bi_2O_4 (JCPDS No. 50-0864). Because of the very small content of BiOCl (or TiO_2) in the hybrid film (the atom ratio of element Zn and Bi is 100:3), it is very difficult to detect the characteristic diffraction peaks of BiOCl (or TiO_2) (Figure S2, Supporting Information). In order to confirm the existence of BiOCl (or TiO_2), X-ray photoelectron spectra (XPS) was used to examine the element condition on the surface of the hybrid films. Figure 2b shows survey scan XPS spectra of the prepared BiOCl/ZnO film and TiO_2/ZnO film. The signals of Zn 2p are readily observed in all the samples. The weak peaks for Bi (or Ti) also suggest the small content of BiOCl (or TiO_2) in the hybrid films. Figure 2c,d shows the high-resolution XPS spectra of Bi 4f and Ti 2p peaks, respectively. Two strong peaks at 159.4 and 164.6 eV are assigned to Bi $4f_{7/2}$ and Bi $4f_{5/2}$, which correspond to Bi^{3+} in BiOCl[29] (Figure 2c). Compared with the standard bind energy data, the peaks have little shift, which maybe result from the calcination treatment at 450 °C. The characteristic peak of Ti 2p in the TiO_2/ZnO hybrid film is not significant, which may be caused by the shelter of ZnO nanoparticles and the aggregation of TiO_2 nanoparticles, but the peak at 460 eV can still confirm the existence of TiO_2.

Figure 3 shows the UV–vis absorption spectra of all the three films. The ZnO film shows a cutoff wavelength at 380 nm due to the band edge absorption of ZnO NPs. After the incorporation of BiOCl (or TiO_2), the absorbance for the hybrid film in UV-A region largely increases, which may be caused by the absorption of BiOCl nanoclusters (E_g = 3.1 eV, Figure S3, Supporting Information) (or TiO_2 NPs), and the rough surface of the hybrid films. Room temperature photoluminescence (PL) measurement of the three films was carried out using a Xe lamp as the source with the excitation wavelength at 314 nm, and the results are shown in Figure 3b. The luminescence intensity of both BiOCl/ZnO hybrid film and TiO_2/ZnO hybrid film reduces significantly compared with that of pristine ZnO film, indicating that the incorporation of BiOCl (TiO_2) can effectively inhibit the recombination rate of photoinduced carriers in ZnO film. As shown in Figure 3c, the PL signal can be fitted by Gaussian function into three bands centered around 380,

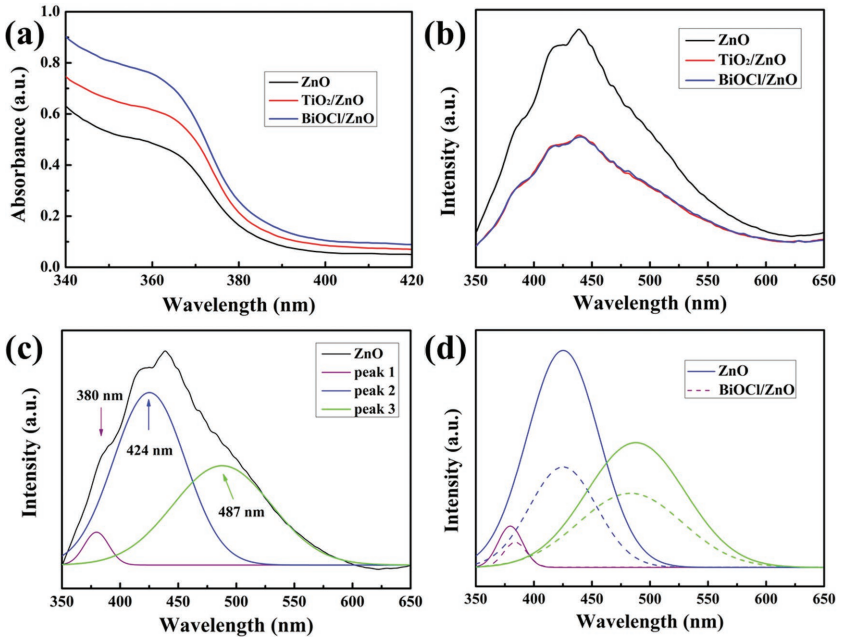

Figure 3. a) UV–vis absorption spectra and b) PL spectra of the obtained three films. c) Gaussian-fitted PL spectrum of ZnO film. d) Comparison of the fitting spectra of ZnO and BiOCl/ZnO film.

424, and 480 nm, corresponding to the band edge emission of ZnO, interstitial Zn, and oxygen vacancies on the surface, respectively.[30,31] The interstitial Zn may be caused by the movement of Zn ions, resulting from the large amount of oxygen vacancies, which is caused by the carbonization of poly(vinyl alcohol) (PVA) during the calcination process. A comparison of the fitted PL peaks between ZnO and BiOCl/ZnO reveals that the BiOCl can enrich the holes in the hybrid film and reduce the recombination of photogenerated electrons and holes (Figure 3d).

The obtained ZnO film, TiO_2/ZnO film, and BiOCl/ZnO film were constructed into PDs with two pieces of silver paste as the electrodes. The current–voltage (*I–V*) curves of all the three PDs in semilogarithmic coordinate in the dark and upon 350 nm (0.15 mW cm^{-2}) UV light illumination are displayed in **Figure 4**a. The current of ZnO film PD increases remarkably from 30 pA (dark condition) to 20 nA under 350 nm UV light illumination at an applied voltage of 5.0 V. Compared with the ZnO film PD in our previous work,[27] the ZnO film PD in this study exhibits lower dark current due to its loose and porous structure, which leads to more oxygen molecules adsorbed on the ZnO NPs. The initial on/off ratio of this PD can reach 10^3, implying that ZnO is a good candidate to develop high performance photoconductive detector. When incorporating TiO_2 clusters in the ZnO film (SEM image in Figure 1d), the current under 350 nm UV light illumination increases, while the dark current almost remains the same. The increase of current under illumination may be caused by the desorption of oxygen molecules, resulting from the hole injection of TiO_2. Interestingly, when the BiOCl nanostructures were inserted in the ZnO film, the current under illumination greatly increases and the dark current reduces significantly. The enhanced current may be caused by the injection of electrons from BiOCl to ZnO, and the reduced dark current may be caused by the barriers formed on the electron transport path between electrodes.

The responsivity defined as photocurrent per unit of incident power, is also important to evaluate the performance of PDs, which is usually calculated using the equation:[8,32,33]

$$R_\lambda = (I_\lambda - I_d)/(P_\lambda S) \quad (1)$$

where I_λ is the measured current at certain wavelength, I_d is the dark current, P_λ is light power density, and S is the photosensitive area, which is about 0.5 mm^2 for our devices. Figure 4b shows the spectral response characteristics of all the three PDs at 5 V bias. Sharp cutoff wavelength occurs at 370 nm for both ZnO film PD and TiO_2/ZnO hybrid film PD. The responsivity of the fabricated TiO_2/ZnO film PD under illumination of 350 nm is 67.06 mA W^{-1}, which is 1.37 times higher than that of ZnO film PD (28.25 mA W^{-1}). The cutoff edge of BiOCl/ZnO film PD is about 380 nm, mainly ascribing to the generation of Bi_2O_4 after calcination at 450 °C. Its responsivity at 350 nm can reach 182.87 mA W^{-1}, which is 2.72 and 6.87 times for that of TiO_2/ZnO film PD and ZnO film PD, respectively. The UV–visible rejection ratio defined as $R_{350\ nm}/R_{500\ nm}$ is about 907.1 for the BiOCl/ZnO film PD, which reduced by 15% and 38% compared with the ZnO film PD and TiO_2/ZnO film PD, respectively, possibly resulting from the visible light absorption of the product of BiOCl after calcination at 450 °C.

Time-dependent current (*I–t*) curve is measured with periodical on/off UV light illumination at 5 V bias, as shown in Figure 4c. High stability and repeatability were achieved with five cycles of switching on and off upon 350 nm UV light with a power density of 0.15 mW cm^{-2}. The initial on/off ratios (the first cycle) of the ZnO film PD, TiO_2/ZnO PD, and BiOCl/ZnO film PD are about 10^3, 10^3, and $>10^4$, respectively, while the stable on/off ratios (the third cycle) of the three PDs are 7.8, 52.54, and 798.3, respectively, which are determined by the decay time. Figure 4d compares the normalized time-dependent photocurrents under 5 V bias. The rise and decay times of ZnO film PD are 69.34 and >120 s, respectively (the rise time is defined as the time for the current to raise to 90% of the peak value and the decay time is defined as the time for the current to decay to 10% of the peak value). By comparison, both the BiOCl/ZnO film PD and TiO_2/ZnO film PD exhibit shorter rise/decay time (25.83/11.25 s and 51.94/26.05 s). The large difference in improvement can be attributed to the intrinsic characteristics of BiOCl and TiO_2. For the TiO_2/ZnO film PD, because the potential value of the valance band edge of TiO_2 is more positive than that of ZnO (vs. NHE),[34–36] photogenerated holes would be injected into the ZnO film under UV light illumination,

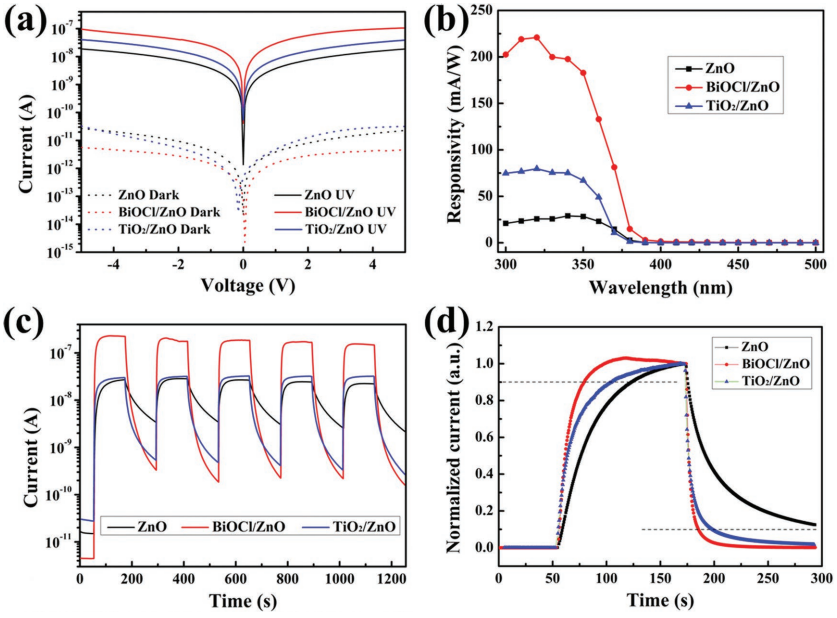

Figure 4. Typical photodetection tests of all the three obtained PDs based on ZnO film, BiOCl/ZnO hybrid film, and TiO_2/ZnO hybrid film. a) *I–V* curves under dark and 350 nm UV light illumination. b) Responsivity spectra. c) Time-dependent photocurrent curves at 5 V bias under 350 nm UV light illumination and d) the corresponding normalized *I–t* curves.

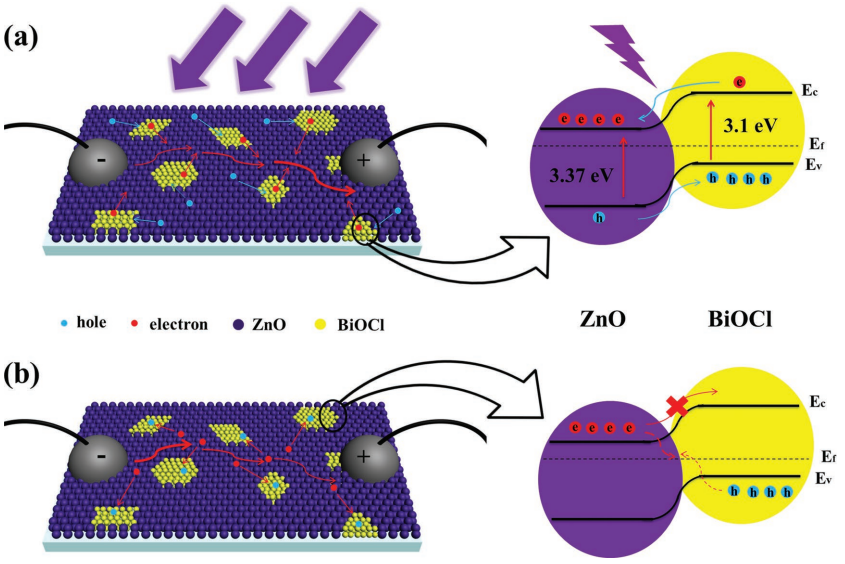

Scheme 1. The schematic illustration of the transfer process and the energy levels of BiOCl/ZnO film PD a) under and b) without UV light illumination.

which can accelerate the desorption of oxygen molecules, resulting in the increase of photocurrent. Meanwhile, the photogenerated electrons would transport from ZnO to TiO_2, causing the decrease of decay time. When the UV light is turned off, the electrons in the ZnO film would transport into the TiO_2 clusters and recombine with the holes on the surface of TiO_2 particles. Then, the current attenuation process was accelerated and short decay time is obtained. On the other hand, as a typical p type semiconductor material, when BiOCl contacts with ZnO, p–n junction is formed at the interface, leading to a built-in electric field formed between BiOCl and ZnO. The electrons in BiOCl would transport into ZnO, while the hole transfers in the opposite direction under UV light illumination. This process greatly increases the concentration of free carries in the ZnO film, thus leading to the increase of photocurrent, as illustrated in **Scheme 1**a. When the UV light is turned off, holes on the BiOCl clusters would migrate to the interface between BiOCl and ZnO particles and recombine with the electrons in the ZnO film. Meanwhile, the built-in electric field would block the straight transmission of electrons and force them to bypass, which extend the diffuse distance of electrons, thus resulting in the decrease of decay time, as illustrated in Scheme 1b.

Considering that the chemical composition and crystal phase of BiOCl would change after high temperature treatment, the BiOCl/ZnO film calcined at different temperatures have been prepared and constructed as PDs. **Figure 5**a shows the XRD patterns of BiOCl nanosheets calcined at different temperatures. It can be observed that the sample calcined at 400 °C is a typical tetragonal structure of BiOCl, while small amount of Bi_2O_4 is formed at 450 °C. Bi_3O_4Cl is formed when the temperature reaches 500 °C. And large amounts of Bi_3O_4Cl emerge in the sample calcined at 550 °C.[29] The *I–V* curves of the BiOCl/ZnO film PDs calcined at different temperatures under UV light (350 nm) illumination have been shown in Figure 5b. The *I–t* curves of the obtained samples at 5 V bias under UV light illumination are shown in Figure 5c. When the calcination temperature is below 500 °C, the photocurrent of BiOCl/ZnO film PD basically keeps constant, while significant decline appears when the calcined temperature goes up to 550 °C. The photocurrent decrease may be caused by the generation of Bi_3O_4Cl. The appearance of Bi_3O_4Cl also leads to the increase of decay time. From the normalized time-dependent photocurrent curves (Figure 5d), the rise/decay time of BiOCl/ZnO film PD calcined at 450 °C is 28.5/11.2 s (Table S1, Supporting Information), which is much shorter than that of PDs calcined at other temperatures.

As the BiOCl clusters can inject electrons into ZnO film and draw holes from ZnO film, resulting in the generation of high photocurrent, the content of BiOCl in the hybrid film plays an important role in the performance enhancement of BiOCl/ZnO film PDs. Therefore, BiOCl/ZnO films with different BiOCl contents (Zn:Bi = 100:*x*, *x* = 1, 2, 3, 4, 5) have been prepared to study the influence of BiOCl content. **Figure 6** shows the results of typical photodetection measurements for a series of samples with different BiOCl

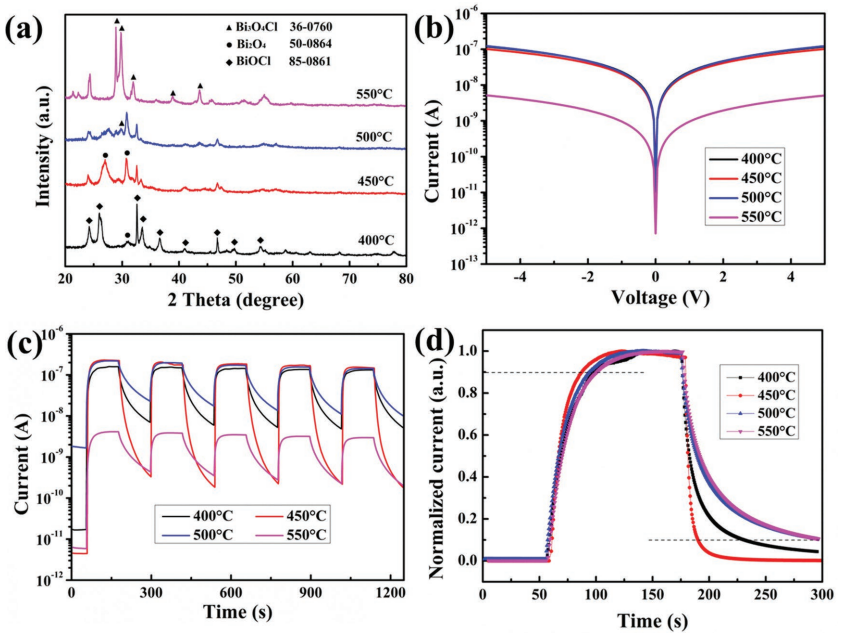

Figure 5. a) The XRD patterns of BiOCl nanosheets calcined at different temperatures. b) *I–V* curves, c) *I–t* curves at 5 V bias, and d) their corresponding normalized *I–t* curves of BiOCl/ZnO hybrid film PDs calcined at different temperatures.

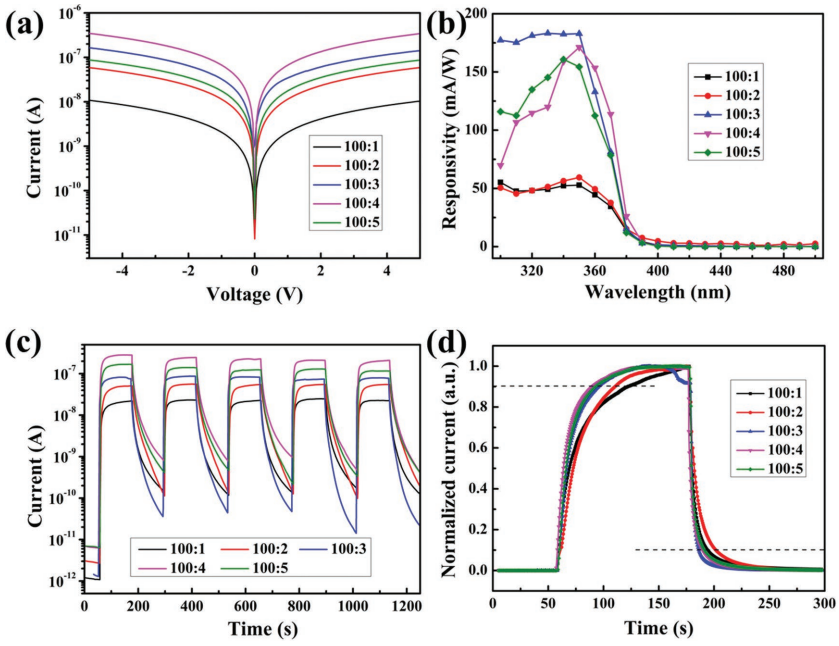

Figure 6. Typical photodetection tests of the BiOCl/ZnO hybrid film PDs with different BiOCl contents. a) *I–V* curves under 350 nm UV light illuminations. b) Responsivity spectra at 5 V bias. c) Time-dependent photocurrent curves at 5 V bias under UV light illumination. d) Corresponding normalized *I–t* curves.

contents. The *I–V* curves (Figure 6a) indicate that the photocurrent of the hybrid film PD with the atomic ratio of 100:1 slightly decreases compared with that of the pristine ZnO film PD, owing to the addition of few amount of BiOCl and the distortion of the flat film. For the other PDs, the photocurrent increases as the content of BiOCl increases, except the one with the highest loading of BiOCl (100:5), which shows lower photocurrent than that of 100:4 PD. Figure 6b shows the responsivity spectra of the hybrid film PDs, which reveals that the responsivity also increases as the BiOCl content increases when the ZnO:BiOCl ratio is below 100:3. When the ratio is over 100:3, the responsivity of the hybrid film PDs decreases gradually, and it exhibits UV-A response to some extent simultaneously. Figure 6c presents the *I–t* curves of the PDs when the UV light is switched on/off every 120 s, at a constant bias voltage of 5.0 V. All these devices can be switched repeatedly with the on/off ratio of about 10^3 and demonstrate good stability. From the normalized *I–t* curves, the rise/decay time decreases first and then increases with the increase of BiOCl content, as listed in **Table 1**. The decrease of rise/decay time for the 100:1, 100:2, and 100:3 PDs is mainly caused by the generation of barriers between electrodes, resulting from the BiOCl clusters. While, the increase of rise/decay time for 100:4 and 100:5 PDs is possibly caused by the excess barriers between electrodes, which greatly blocks the transport path of electrons between electrodes, and this phenomenon can also be confirmed in the BiOCl/ZnO film PD with high content of BiOCl (Figure S4, Supporting Information). These results demonstrate that certain content of BiOCl can improve the photocurrent response and decrease the rise/decay time synchronously, leading to the enhanced performance of ZnO film PDs.

All the experiment results aforementioned demonstrate that the emergence of electron barriers formed by BiOCl clusters are the main reason for the decrease of rise/decay time, which is different from controlling the depletion layer on the surface of ZnO particles to improve the performance of ZnO film PDs. In order to investigate whether these two methods can work synergistically or not, gold nanoparticles were deposited on the surface of BiOCl/ZnO film (sample 100:3) by ion-sputtering method for different times. **Figure 7**a shows the photocurrent of the obtained PDs under 350 nm UV light illumination. After gold nanoparticle deposition, the photocurrents become smaller than that of the pristine ZnO film PD, which indicates that the modification of gold nanoparticles cannot increase the photocurrent of BiOCl/ZnO film PDs. The results of responsivity spectra agree well with the change of photocurrent, as shown in Figure 7b. The *I–t* curves (Figure 7c) and normalized *I–t* curves (Figure 7d) of the BiOCl/ZnO film PDs after gold NP decoration exhibit excellent stability and shorter rise/decay time. Meanwhile, the ZnO film PDs with gold NP modification show the same trend (Figure S5, Supporting Information), which implies that the combination of BiOCl cluster and gold NPs in the film does not result in the enhancement of optoelectronic performance. It is because that the gold NPs on the surface of both ZnO NPs and BiOCl NPs would obstruct the transport path of electrons from BiOCl to ZnO and lead to the decrease of photocurrent for the hybrid PDs.

Table 1. The characteristic parameters for all the PDs prepared in this study.

Photodetector	Responsivity [mA W^{-1}]	On/off ratio (stable)	UV–visible rejection	Rise time [s]	Decay time [s]
ZnO film	28.3	7.8	1070	69.34	>120
TiO_2/ZnO film	67.1	52	1461	51.94	26.05
BiOCl/ZnO 100:1	53.0	398	870	66.06	16.31
BiOCl/ZnO 100:2	58.9	408	990	49.75	24.07
BiOCl/ZnO 100:3	182.2	798	907	29.23	11.20
BiOCl/ZnO 100:4	169.3	337	3423	34.22	12.82
BiOCl/ZnO 100:5	153.6	395	3088	35.14	13.49

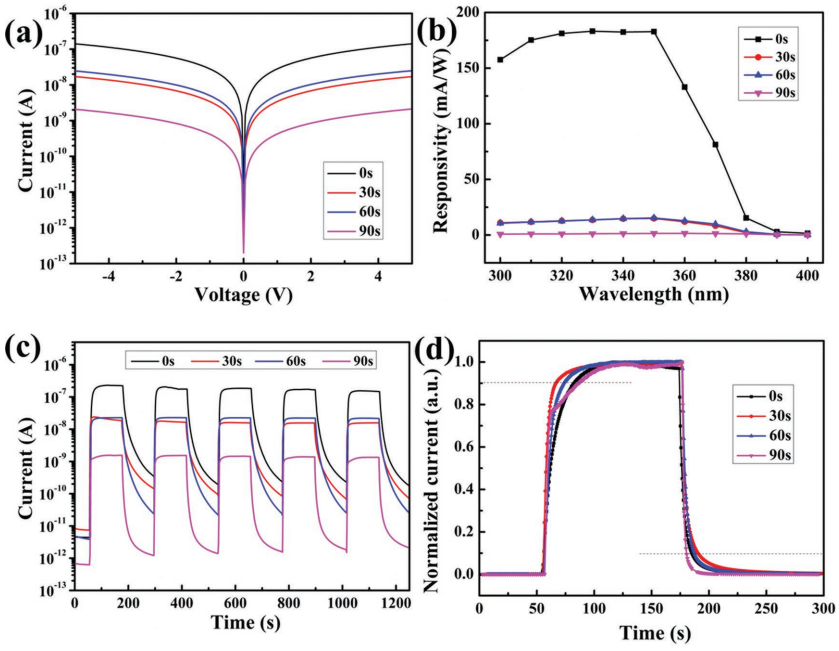

Figure 7. Typical optoelectronic tests of the Au NP modified BiOCl/ZnO hybrid film PDs with different sputtering times. a) *I–V* curves under 350 nm UV light illuminations. b) Responsivity spectra at 5 V bias. c) Time-dependent photocurrent curves at 5 V bias under UV light illumination and d) the corresponding normalized *I–t* curves.

3. Conclusion

In summary, a series of novel BiOCl/ZnO hybrid film structures were facilely prepared and constructed as film PDs. Compared with the pristine ZnO film PD and TiO_2/ZnO hybrid film PD, the BiOCl/ZnO film PDs exhibit higher photocurrent and shorter rise/decay time, owing to the formation of p–n junction between the BiOCl and ZnO. The BiOCl clusters in the film not only injects electrons into the ZnO film under UV light illumination, but also form barriers to block the straight transport path of electrons between electrodes when the UV light is turned off, which leads to the increase of photocurrent and the decrease of decay time. However, excess BiOCl clusters in the hybrid film would significantly block the transport path of electrons between electrodes, resulting in the decrease of photocurrent. As the crystal phase of BiOCl changes when the calcination temperature is over 500 °C, the hybrid film PD calcined at different temperatures was prepared to examine the temperature effect. The physical mechanism for the reduced decay time and the increased photocurrent of the hybrid film PDs is well investigated, which is different from those methods that enhance the performance of PDs by adjusting the depletion layer on the surface of ZnO NPs. The BiOCl/ZnO hybrid structure film PD provides a new and simple route for the enhancement of optoelectronic performance based on the ZnO nanostructures.

4. Experimental Section

Preparation of the BiOCl/ZnO Film: The BiOCl nanosheets were synthesized by hydrothermal method, and the detail processes are presented in the Supporting Information. The procedures of fabricating BiOCl/ZnO hybrid films and ZnO films were described as follows: ZnO precursor solution was formed by dissolving 1.44 g of $Zn(CH_3COO)_2 \cdot 2H_2O$ and 0.75 g of PVA-1788 (low-viscosity, $M_w = 44.05$) into a mixture of 10 mL of water/alcohol solution (v/v = 9:1) and 0.5 mL of CH_3COOH. The pure ZnO film was prepared by spin-coating the precursor solution on a glass substrate twice at 3000 rpm for 20 s, and then being annealed in air at 450 °C for 2 h. In order to uniformly disperse the BiOCl nanosheets in the ZnO film, 700 mg of BiOCl nanosheets were dispersed in 10 mL of analytically pure alcohol, and ultrasonicated for 10 h. Then, the BiOCl dispersion solution was added into the ZnO precursor solution drop by drop under continuous stirring. For comparison, hybrid films with different BiOCl contents (Zn:Bi = 100:*x*, *x* = 1, 2, 3, 4, 5) and calcined at different temperatures (400, 500, and 550 °C) were prepared to investigate the influence of BiOCl.

Analysis Instruments: The morphologies of samples were characterized using a field-emission scanning electron microscopy (Zeiss Sigma) and atomic force microscopy (AFM) (Bruker, MultiMode-8). X-ray diffraction patterns were collected on a Bruker D8-A25 diffractometer using Cu Kα radiation (λ = 1.5405 Å). The XPS spectra of the samples were recorded by a Perkin Elmer PHI 5000 °C ESCA system equipped with a hemispherical electron energy analyzer, and the Mg-Kα (1253.6 eV) anode was operated at 14 kV and 20 mA. All the binding energy for C 1s peak at 284.6 eV was used as the reference for calibration. The optical properties were investigated by optical absorption spectra using a UV–vis spectrophotometer (Hitachi U-3900H) with an integrating sphere attachment. PL emission spectra were recorded under ambient conditions (FLS 920 Edinburgh instruments) with an excitation wavelength at 314 nm using a Xe lamp as the excitation source.

Photoelectric Measurements: To construct the photodetector device, two small pieces of silver pastes with areas of about 0.5 mm^2 were placed onto the films as electrodes. The photodetection performance was analyzed with a 450 W Xe lamp, monochromator, a program-controlled semiconductor characterization system (Keithley 4200, USA). The light intensity was measured with a NOVA II power meter (OPHIR photonics). All the measurements were performed at room temperature.

Supporting Information

Supporting Information is available from the Wiley Online Library or from the author.

Acknowledgements

This work was supported by the National Natural Science Foundation of China (Grant Nos. 11674061 and 51471051), the National

Postdoctoral Science Foundation of China (2016M591603), the Science and Technology Commission of Shanghai Municipality (15520720700), and the Shanghai Shu Guang Project (12SG01), and the Programs for Professor of Special Appointment (Eastern Scholar) at Shanghai Institutions of Higher Learning. Part of this work was carried out in the Fudan Nano-fab Laboratory.

Conflict of Interest

The authors declare no conflict of interest.

[1] N. Nasiri, R. Bo, T. F. Hung, V. A. L. Roy, L. Fu, A. Tricoli, *Adv. Funct. Mater.* **2016**, *26*, 7359.
[2] H. Y. Chen, K. W. Liu, L. F. Hu, A. A. Al-Ghamdi, X. S. Fang, *Mater. Today* **2015**, *18*, 493.
[3] L. Peng, L. F. Hu, X. S. Fang, *Adv. Mater.* **2013**, *25*, 5321.
[4] L. Ding, N. Liu, L. Li, X. Wei, X. Zhang, J. Su, J. Rao, C. Yang, W. Li, J. Wang, H. Gu, Y. Gao, *Adv. Mater.* **2015**, *27*, 3525.
[5] X. Li, C. Gao, H. Duan, B. Lu, Y. Wang, L. Chen, Z. Zhang, X. Pan, E. Xie, *Small* **2013**, *9*, 2005.
[6] Y. R. Xie, L. Wei, G. D. Wei, Q. H. Li, D. Wang, Y. X. Chen, S. S. Yan, G. L. Liu, L. M. Mei, J. Jiao, *Nanoscale Res. Lett.* **2013**, *8*, 188.
[7] X. S. Fang, L. F. Hu, K. F. Huo, B. Gao, L. J. Zhao, M. Y. Liao, P. K. Chu, Y. Bando, D. Golberg, *Adv. Funct. Mater.* **2011**, *21*, 3907.
[8] H. Liu, Z. M. Zhang, L. F. Hu, N. Gao, L. W. Sang, M. Y. Liao, R. Z. Ma, F. F. Xu, X. S. Fang, *Adv. Opt. Mater.* **2014**, *2*, 771.
[9] A. B. Djurišić, A. M. C. Ng, X. Y. Chen, *Prog. Quantum Electron.* **2010**, *34*, 191.
[10] Z. Wang, R. Yu, X. Wang, W. Wu, Z. L. Wang, *Adv. Mater.* **2016**, *28*, 6880.
[11] W. Dai, X. Pan, S. Chen, C. Chen, Z. Wen, H. Zhang, Z. Ye, *J. Mater. Chem. C* **2014**, *2*, 4606.
[12] T. P. Chen, F. Y. Hung, S. P. Chang, S. J. Chang, Z. S. Hu, K. J. Chen, *Appl. Phys. Express* **2013**, *6*, 045201.
[13] Q. Xu, Q. Cheng, J. Zhong, W. Cai, Z. Zhang, Z. Wu, F. Zhang, *Nanotechnology* **2014**, *25*, 055501.
[14] C. Soci, A. Zhang, B. Xiang, S. A. Dayeh, D. P. R. Aplin, J. Park, X. Y. Bao, Y. H. Lo, D. Wang, *Nano Lett.* **2007**, *7*, 1003.
[15] A. Manekkathodi, M. Y. Lu, C. W. Wang, L. J. Chen, *Adv. Mater.* **2010**, *22*, 4059.
[16] Z. Jin, Q. Zhou, Y. Chen, P. Mao, H. Li, H. Liu, J. Wang, Y. Li, *Adv. Mater.* **2016**, *28*, 3697.
[17] H. Chen, K. Liu, X. Chen, Z. Zhang, M. Fan, M. Jiang, X. Xie, H. Zhao, D. Shen, *J. Mater. Chem. C* **2014**, *2*, 9689.
[18] M. Zhao, X. Wang, G. Yang, M.-Y. Zhou, W.-J. Liu, T.-W. Luo, H.-F. Tan, X.-R. Sun, *Appl. Surf. Sci.* **2015**, *359*, 432.
[19] Q. H. Li, T. Gao, Y. G. Wang, T. H. Wang, *Appl. Phys. Lett.* **2005**, *86*, 123117.
[20] Y. Jin, J. Wang, B. Sun, J. C. Blakesley, N. C. Greenham, *Nano Lett.* **2008**, *8*, 1649.
[21] D. Gedamu, I. Paulowicz, S. Kaps, O. Lupan, S. Wille, G. Haidarschin, Y. K. Mishra, R. Adelung, *Adv. Mater.* **2014**, *26*, 1541.
[22] A. Bera, D. Basak, *ACS Appl. Mater. Interfaces* **2010**, *2*, 408.
[23] K. Liu, M. Sakurai, M. Liao, M. Aono, *J. Phys. Chem. C* **2010**, *114*, 19835.
[24] A. Bera, D. Basak, *ACS Appl. Mater. Interfaces* **2009**, *1*, 2066.
[25] Y. Wu, B. Yuan, M. Li, W.-H. Zhang, Y. Liu, C. Li, *Chem. Sci.* **2015**, *6*, 1873.
[26] J. Li, Y. Yu, L. Zhang, *Nanoscale* **2014**, *6*, 8473.
[27] F. Teng, L. X. Zheng, K. Hu, H. Y. Chen, Y. M. Li, Z. M. Zhang, X. S. Fang, *J. Mater. Chem. C* **2016**, *4*, 8416.
[28] F. Teng, G. Zhang, Y. Wang, C. Gao, L. Chen, P. Zhang, Z. Zhang, E. Xie, *Appl. Surf. Sci.* **2014**, *320*, 703.
[29] Y. Myung, F. Wu, S. Banerjee, A. Stoica, H. Zhong, S.-S. Lee, J. Fortner, L. Yang, P. Banerjee, *Chem. Mater.* **2015**, *27*, 7710.
[30] B. J. Jin, S. Im, S. Y. Lee, *Thin Solid Films* **2000**, *366*, 107.
[31] Z. Fang, Y. Wang, D. Xu, Y. Tan, X. Liu, *Opt. Mater.* **2004**, *26*, 239.
[32] L. X. Zheng, F. Teng, Z. M. Zhang, B. Zhao, X. S. Fang, *J. Mater. Chem. C* **2016**, *4*, 10032.
[33] L. X. Zheng, P. P. Yu, K. Hu, F. Teng, H. Y. Chen, X. S. Fang, *ACS Appl. Mater. Interfaces* **2016**, *8*, 33924.
[34] P. Tiwana, P. Docampo, M. B. Johnston, H. J. Snaith, L. M. Herz, *ACS Nano* **2011**, *5*, 5158.
[35] T. J. Athauda, J. G. Neff, L. Sutherlin, U. Butt, R. R. Ozer, *ACS Appl. Mater. Interfaces* **2012**, *4*, 6917.
[36] F. X. Xiao, *ACS Appl. Mater. Interfaces* **2012**, *4*, 7055.

Received: January 12, 2017
Revised: February 24, 2017
Published online: April 18, 2017

